Use of virtual sensors for the analysis of forces exerted by the load inside a tumbling mill

José Venegas Pulgar[1], M. Aníbal Valenzuela[2] and Cristián Molina Vicuña[1]

[1]Laboratorio de Vibraciones Mecánicas, Departamento de Ingeniería Mecánica,
Universidad de Concepción, Chile
{jvenegasp, crimolin}@udec.cl
[2]Laboratorio de Accionamientos Eléctricos, Departamento de Ingeniería Eléctrica,
Universidad de Concepción, Chile
anivalenz@udec.cl

Abstract

In this paper, a methodology is presented to obtain average representative forces exerted by the load inside a tumbling mill on the different faces of the lifters and liners, which are directly related to its power consumption. The methodology is based on the use of virtual sensors included in DEM simulations combined with signal processing and allows obtaining the magnitude of the forces based on the angular position of the lifters as the mill rotates. The methodology is validated by comparing numerical and experimental results obtained from a test bench mill. The variables considered are the power, movement of the load inside the mill, and average forces. The latter are experimentally measured using instrumented lifters specially designed for this task. The results obtained show differences in the magnitude of the average forces in specific angular positions, depending on the operating conditions of the mill. These differences explain the behavior of power consumption with respect to operating conditions reported in the literature.

1 Introduction

Tumbling mills are critical machines of the mining industry. They are used to reduce the size of mineral particles, and their operation has associated high economic costs. The grinding of minerals requires high energy consumption and represents the most expensive stage in the production of metals. The economies of scale and the decrease in the grade of the ores, has led to the development of large grinding mills that currently reach throughput of 80,000 - 100,000 ton/day with powers of up to 28 [MW] [1][2].

The main component of the mill is the horizontal hollow cylinder called drum, inside which the ore is grinded (Figure 1a). The drum rotates on its axis and is delimited at its sides by two ends through which occurs the entry and exit of the material, respectively. Fixed to the inner wall of the drum are the coatings, composed by liners and lifters. The liners protect the drum from wear due to contact with the particles, while the lifters transmit the energy associated with the rotation of the mill to the load, producing its movement inside the mill. The comminution of the mineral occurs due to the contact forces that are generated between different particles and between particles and the internal surfaces of the drum.

The liners and lifters wear out over time as a result of the continuous contact with the particles inside the mill. The replacement of these elements constitute the primary maintenance operations and generate high costs associated not only with the purchase of replacement parts and labor but also with production losses during

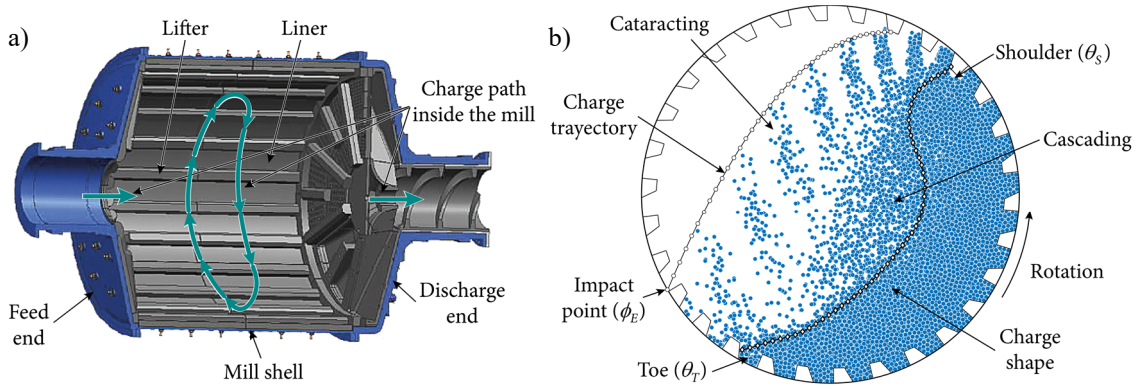

Figure 1: Tumbling mill. (a) General view of the drum. (b) View of the load inside the drum.

maintenance works. In addition, the continuous wear of the coatings produces changes in the power consumption and throughput of the mills.

While rotating, the drum lifts the grinding load along one side of the mill until reaching the point called shoulder of the load, as shown in Figure 1b. In this position, the particles located near the lifters begin to move independently of the movement of the drum and then fall describing free fall movements called cascade type or cataract type. The particles that describe cascade movements from the shoulder characterize by falling continuously, while those that describe cataract movements do so in the form of waves driven by the lifters. In the movement that describes the load inside the mill, a set of relevant angular positions, measured with respect to its axis of rotation, are identified: the position of the shoulder (θ_S), the position of the point of impact (ϕ_E) and the position of the toe (θ_T). The point of impact corresponds to the highest position at which the particles fall from the shoulder on the opposite end of the mill ring. The position of the toe is where the lifters begin to lift the load after it falls from the shoulder.

Figure 1b presents an example of the disposition of the particles inside the mills, showing the shape and trajectory of the load, the position of the toe, of the shoulder, and the point of impact. The shape of the load corresponds to the shape adopted by the set of particles that do not fall in free fall (cascading or cataracting) while the mill rotates, which commonly compares to the shape of a kidney bounded at its ends by the toe and the shoulder. Most of the particles fall from the areas near the shoulder on the internal surface of the shape of the kidney, describing a cascade-type movement, as can be seen in Figure 1. The lifters lift a portion of the particles in the shoulder to higher positions and then fall on the toe or the coatings of the drum near the toe describing a cataract movement. The lifters that leave the position of the shoulder drag small portions of particles that become independent from it gradually, forming waves of particles that are thrown into the free space inside the drum. The formation of these waves then depends on the passage of the lifters out of the shape of the load and, therefore, the impacts of the particles that describe a cataract movement on the area near the toe are not continuous, but linked to the movement of lifters. The trajectory of the load corresponds to the free fall movement that describes the particle that reaches the point of impact.

The Discrete Elements Method (DEM) is a numerical methodology that describes the behavior of granular materials. It allows simulating the movement of each of the particles forming the grinding load inside the mill by modeling the interactions between the different particles and between particles and surfaces, and solving the equations of motion of each particle. DEM has been used by multiple researchers to study tumbling mills focused on, for example, the analysis of the load movement [2][3][4][5][6][7][8][9][10][11][12][13][14][15][16][21][23][26][27][28][32][33][34][45], the study of wear of coatings [2][14][15][30][43][44] and the modeling of the comminution process [16][5][8][17][18][19][20][22][31][35][37][38][39][40][41][42]. This paper focuses on analyzing the power requirements of the mills, a topic that has also been discussed in the literature [13][14][45][49][21][24][25][26][29][33]. Different from other researches, this is done by determining the average forces exerted by the particles on the lifters and liners as a function of the angular position in which they are located. Some studies relate globally the behavior of the load with the contact forces by using different methods [47][48][49][50][51][52][54][55][56]. The correlation between the average forces and the power obtained in this work allows identifying the physical phenomena that explain the observed power variations as a function of the operating conditions.

2 Test bench: SetupD100

The analyses are carried out based on a laboratory scale mill, called SetupD100, shown in Figure 2a. This mill consists of three main components: the ring, a back cover, and a front cover. The ring is a hollow cylinder representing the drum of the mill with lifters mounted on its inside. The ring and lifters are made of technyl. The ring has an internal diameter of 945 [mm], an internal length of 60 [mm] and is delimited at its ends by the back and front cover, respectively. Both covers are made of acrylic. The back cover is gray, while the front is transparent, which allows observing the movement of the load while the mill runs. The mill is connected to the electric drive by a drive shaft in a cantilever arrangement. The drive includes a frequency converter that allows controlling the speed of rotation.

2.1 Lifter geometry

The internal geometry of the mills is one of the main aspects to analyze in order to understand the behavior of the load inside the mill. It is defined mainly by the number of lifters (N_{lft}) and their geometry. Figure 2a shows the dimensions of the lifters installed in the test bench mill.

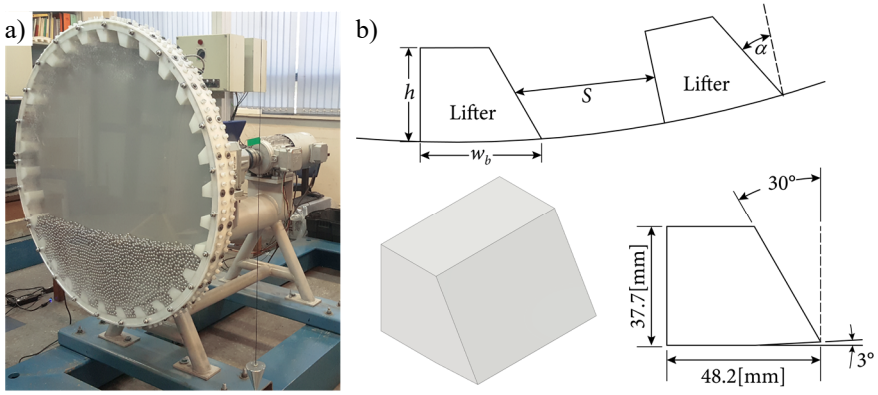

Figure 2: (a) View of the Setup D100. (b) Dimensions of the lifters.

2.2 Operating conditions

The rotating speed and fill level of the mill define its operating condition. The numerical and experimental analyses presented in this paper consider 81 different combinations of speed and fill levels presented in Table 1.

The rotation speed of the mill is defined as a fraction of its critical speed (N). The critical speed of a mill (N_c) corresponds to the speed of rotation from which the load begins to centrifuge, adhering to the internal surfaces of the drum. It is calculated as [47]:

$$N_c = \frac{42.3}{\sqrt{D_M}} \tag{1}$$

The critical speed of the SetupD100 is 4.556 [rad/s], and the 9 speeds analyzed vary from 55% to 95% of it.

The fill level (J_c) is the fraction of the internal volume of the mill that is occupied by the grinding load. The SetupD100 has an internal volume of 0.0396 [m^3] and is filled with 11 [mm] diameter steel balls. The 9 fill levels analyzed range from 25% to 45% of the mill's internal volume, with 2.5% jumps

3 Numerical modeling of the SetupD100

The numerical model of the test bench consists of two main components: a geometric model and a contact model. The geometric model represents the surfaces of the mill with which the particles come into contact, while the contact model describes the interactions between the particles located inside the mill and the components of the geometric model, and between different particles.

3.1 Geometric model of the SetupD100

The geometric model used in this investigation is composed of 3 elements: the ring and the two covers. In the geometric model, the ring and the lifters are considered as a single element. Figure 3a shows the three components of the geometric model, and Figure 3b shows a view of the load inside the mill together with the cartesian system used as a reference for the analyses.

Fraction of the critical speed	Rotation speed, [rad/s]
55%	2.506
60%	2.734
65%	2.961
70%	3.190
75%	3.418
80%	3.645
85%	3.874
90%	4.101
95%	4.329

Fill level	Mass, [kg]
25%	46.25
27.5%	50.87
30%	55.49
32.5%	60.12
35%	64.74
37.5%	69.37
40%	73.99
42.5%	78.61
45%	83.24

Table 1: Operating conditions.

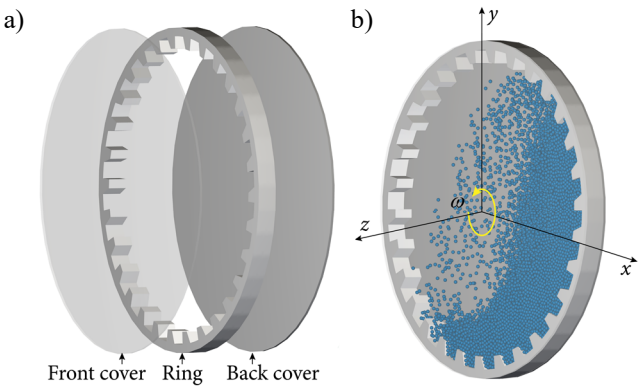

Figure 3: (a) Components of the geometric model. (b) Cartesian reference system.

3.2 Contact model

The particles inside the mill can contact other particles, the covers, or the ring. This means the existence of three different contact types: steel-steel contact between the steel balls, steel-acrylic contact between the steel balls and the acrylic covers, and steel-technyl contact between the steel balls and the ring. The contact models used in DEM allow calculating the forces associated with the contacts to which all the particles are subject, but for this, it is necessary to define the physical parameters that characterize all possible contacts. These parameters are the static friction coefficient, the dynamic friction coefficient, the coefficient of restitution, and the coefficient of rolling resistance. Table 2 shows the values of the contact parameters used in the DEM simulations.

3.3 Power due to the movement of the load inside the mill

Considering the SetupD100 operating as shown in Figure 3b, it can be noted that in any instant of time, not all particles are in contact with the internal surfaces of the mill. It is also noted that a particle can be in contact with the internal surfaces of the mill in more than one point (maximum three) and that there is a given number of contacts (n) between particles and internal surfaces of the mill.

Now, consider a particle that is in contact with one of the internal surfaces of the mill, and that this contact i occurs in a position $\vec{r}_i$ with respect to the axis of rotation of the mill. Let $\vec{F}_i$ be the force exerted by the particle on the point of contact i, as shown in Figure 4a:

$$\vec{r}_i = r_{x,i}\hat{i} + r_{y,i}\hat{j} \tag{2}$$

$$\vec{F}_i = F_{x,i}\hat{i} + F_{y,i}\hat{j} \tag{3}$$

The torque exerted by the particle on the surface at contact i is, thus, given by:

$$\vec{T}_i = \vec{r}_i \times \vec{F}_i \tag{4}$$

Finally, taking into account the n existing contacts between particles and internal surfaces of the mill during a time instant, the torque associated with the movement of the particles inside the mill is given by:

$$\vec{T}_{Mill} = \sum_{i=1}^{n} \vec{T}_i \tag{5}$$

The torque allows to calculate the power due to the operation of the mill at speed ω:

Contact	Coefficient of rolling resistance (μ_r)	Static friction coefficient (μ_s)	Dynamic friction coefficient (μ_k)	Coefficient of restitution (c_R)
	0.01	-	-	-
Steel–Steel	-	0.43	0.36	0.91
Steel–Acrylic	-	0.42	0.38	0.44
Steel – Technyl	-	0.23	0.22	0.69

Table 2: Contact parameters used in the DEM simulations.

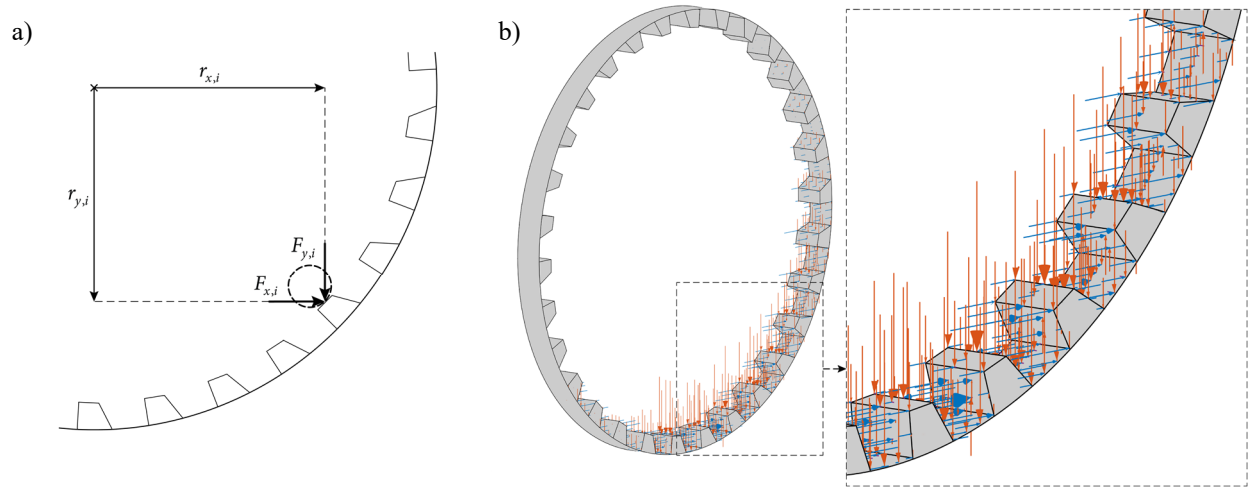

Figure 4: (a) Contact forces of a single particle in contact with the ring. (b) All contact forces acting on the ring with a close view of the contact forces.

$$P_{Mill} = T_{Mill}\omega \tag{6}$$

Thus, the power associated with the movement of the mill originates from the contact between the particles and their internal surfaces. The contacts between the particles contribute to the power indirectly by action/reaction forces, and the Discrete Element Method (DEM) is based on calculating the forces associated with the contacts between particles and between particles and surfaces.

3.3.1 Forces acting on the ring and covers

Figure 4b shows the components of the nodal forces acting on the ring at a given time instant, with a close view of a section of the ring. The blue arrows represent the components of the forces on the *x*-axis; the red arrows represent the components of the forces on the *y*-axis. There are also small purple arrows representing the force components on the *z*-axis. The size of the arrows is scaled based on the magnitude of the forces they represent. As observed, the components of the forces on the *z*-axis are much smaller than the other two components, being so small that they are not recognizable in Figure 4b. The latter, added to the fact that these forces do not contribute to the power, allows treating the analysis of the forces as bidimensional.

Consider the disposition of particles during a given time instant shown in Figure 5a and the forces excerted by these particles on the ring, shown in Figure 5b. It can be seen that the magnitude of the forces exerted by the particles impacting the ring before the toe has a low magnitude and that the amplitude of the forces grows as they come into contact with the ring in the zone between the toe and the shoulder. Also, it is possible to notice that the vertical components of the nodal forces act mainly in the negative direction while the forces in the horizontal direction are positive or negative depending on the face of the lifter in which they act. The sense of the horizontal forces determines the sense of the torque they generate.

Figure 6 shows the forces of Figure 5 decomposed in the ring tangential direction. These components are those that contribute to the torque associated with the movement of the particles. It can be seen that the forces acting on the back face of the lifters (purple arrows) generate torque in the same direction as the rotation of the

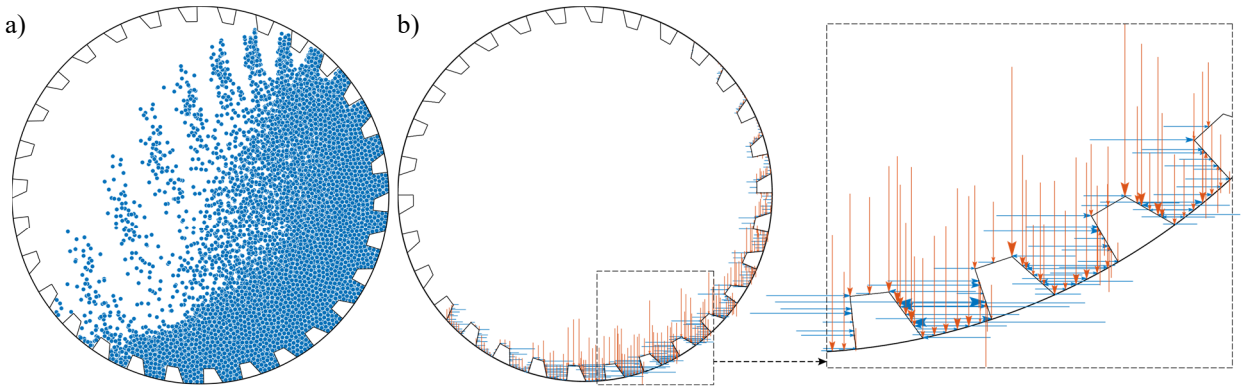

Figure 5: (a) Disposition of particles at a given time instant. (b) Forces excerted by the particles on the lifters and liners at a given instant of time.

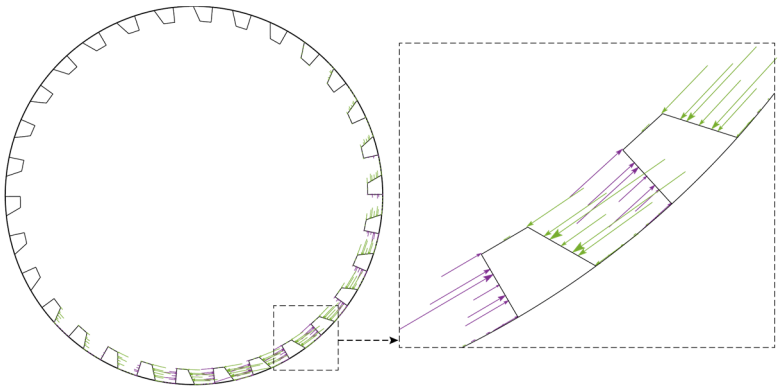

Figure 6: Decomposition of forces in tangential direction.

mill, while the forces acting on the front face of the lifters (green arrows) generate torque in the opposite direction. It is also possible to notice that the components of the forces that contribute to the torque and that act on the liners or the top faces of the lifters are of very low amplitude when compared with the components that act on the front and back faces. Finally, it can be seen that the magnitude of the tangential forces varies significantly with the angular position. In this work, the power associated with the forces exerted by the particles on the ring and obtained using DEM is called $P_{DEM,Ring}$.

The main consequence of this analysis is that, depending on the face of the lifter in which the forces act, they can contribute or oppose the total torque exerted by the load, which determines the required driving torque. The evolution of these forces, depending on the internal geometry of the mill and the operating conditions, have a significant influence on the power consumption associated with its operation.

Figure 7a shows the components of the forces in x-axis and y-axis acting due to friction on one of the acrylic covers of the mill. Figure 7b shows the tangential decomposition of these forces, where the size of the arrows is according to their magnitude. As observed, the forces on the covers that generate torques are of similar magnitude to those acting on the ring. The magnitude of the power associated with the back cover and front cover is similar and, therefore, both covers are treated indistinctly in this work.

The power associated with the movement of both covers is defined as $P_{DEM,Covers}$ and is calculated by adding the powers associated with each cover.

3.3.2 Total power due to the movement of the load inside the mill

The total power associated with the operation of the mill obtained by modeling the SetupD100 using DEM corresponds to the sum of the powers associated with each of its components:

$$P_{DEM,Mill} = P_{DEM,Ring} + P_{DEM,Cover1} + P_{DEM,Cover2} \tag{7}$$

Most of the power associated with the movement of particles inside industrial scale mills comes from the contact forces acting on the liners and lifters. In the case of the power associated with the operation of the SetupD100, both the power associated with the ring and the covers are of similar magnitude because the length of the ring is too short for its diameter.

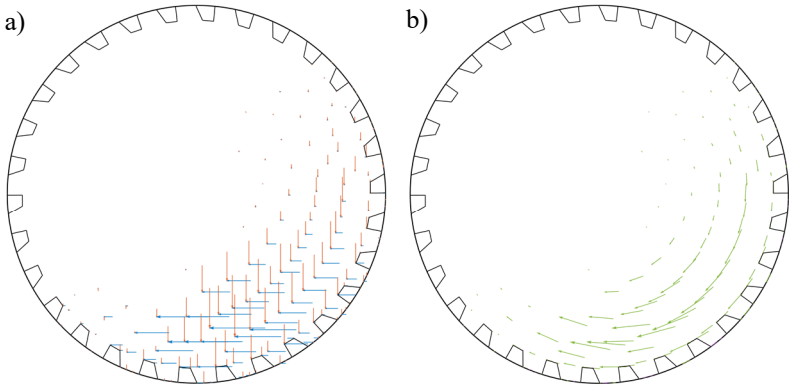

Figure 7: Forces acting on one cover (a) in x and y direction. (b) Tangential decomposition of the forces.

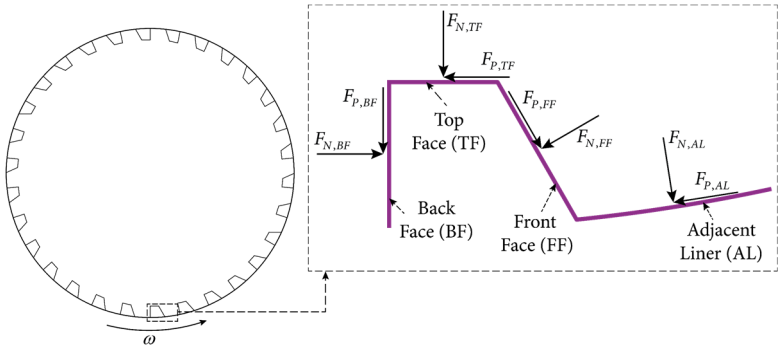

Figure 8: Normal and parallel forces acting on the 3 faces of the lifter and adyacent liner.

4 Model of forces acting on the lifters

As explained in section 3.3.1, the magnitude of the forces exerted by the particles on the ring when the mill rotates depends on the angular position of the liners and lifters, and on the lifter face on which they act. Motivated by this, a force model is developed, based on DEM simulation results. The model allows obtaining the magnitude of the average forces acting on the different faces of the lifters and liners as a function of its angular position θ while the mill operates. This model groups the contact forces exerted by the particles on the liners and each face of the lifters of the mill. The internal geometry of the mill divides into four faces: the front face (FF), the back face (BF), the top face (TF) and the adjacent liner (AL). The forces acting on the ring are divided into 8 forces that act normal and tangential to each face, as shown in Figure 8.

4.1 Modification of the geometric model: implementation of virtual sensors

To obtain the magnitude of the average forces exerted by the particles on the 3 faces of the lifters and adjacent liners as a function of their angular position, a set of three virtual sensors is incorporated in the geometrical model of the DEM model of the SetupD100, as shown in Figure 9a. The virtual sensors (VS) consist of 4 independent sheets (one for each face of the lifter plus the adjacent liner) fixed to the lifters they cover. The fact that the sheets are independent geometries allows obtaining the resultant force exerted by the particles on each sheet as a function of time separately.

Figure 9b shows an example of the forces acting on one of the sheets covering the front face (FF) of the lifter of one of the virtual sensors, as directly obtained from the DEM software, that is, in terms of the *xy*-coordinates. Since there are 3 virtual sensors with their respective 4 sheets, a total of 12 *x* and *y* force signals as a function of time is obtained from each simulation.

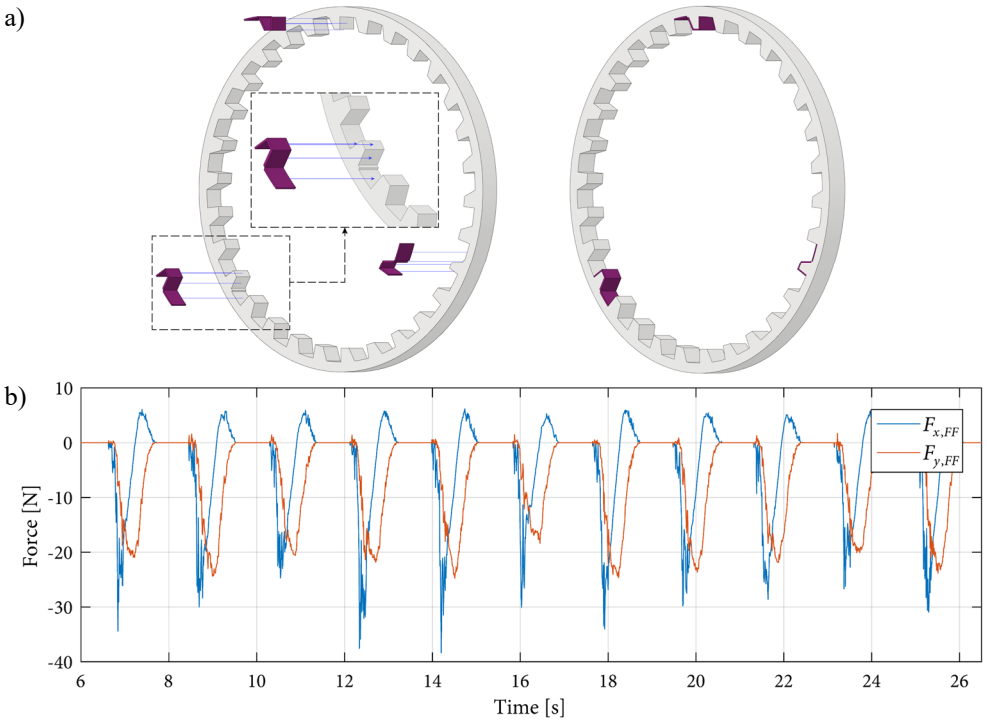

Figure 9: (a) Set of virtual sensors included in the geometric model. (b) Example of time history of force signal in *xy* coordinate for the front face of one lifter.

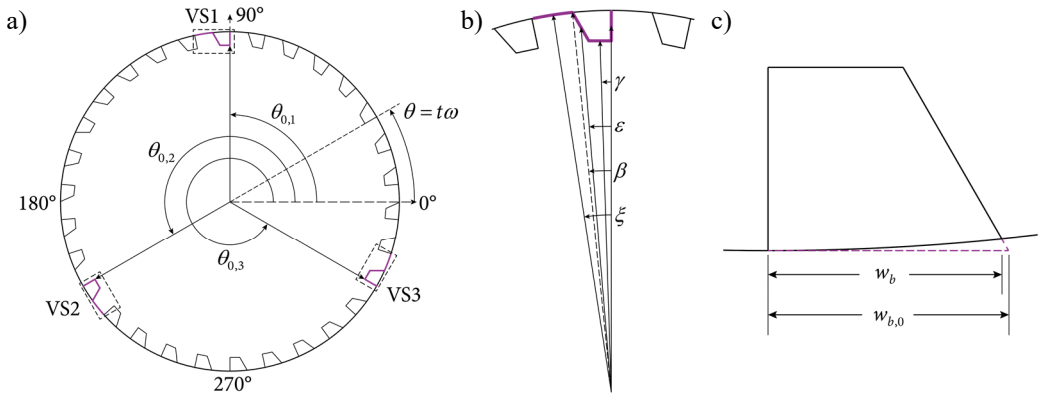

Figure 10: a) Starting position of the virtual lifters. b) Angles used to define the center position of the lifter faces and adjacent liner. c) Projected width of lifter.

4.2 Transformation of forces into local coordinates

The first step in the processing of the forces is to transform the forces captured by the virtual sensors, based on the global *xy* coordinates (Figure 9b), in terms of the local coordinates defined for each face according to Figure 8. The global coordinates are fixed in space so that the mill rotates with respect to the *xy* plane. On the other hand, the virtual sensors move with the lifters on which they are mounted and, consequently, rotate with the mill. Because of this, all local coordinates, defined for each of the faces of the VS, also rotate with the mill. Hence, to transform the forces from global to local coordinates, it is necessary to know the location of each of the faces of the VS as a function of time, based on the rotation of the mill.

4.2.1 Angular displacement equations of virtual sensor faces

In order to know the location of the different faces of the virtual sensors with respect to the axis of the mill, the equations describing the angular displacement of the centers of the 3 lifter faces and adjacent liner are considered. Figure 10a shows the starting position of the three virtual sensors (VS), where the back face of VS1 is located at 90° with respect to the horizontal, that is, $\theta_{0,1} = \pi/2$. The back face of the VS2 and VS3 are located at 120° and 240° from the back face of the SV1, respectively. The angular position of the centers of the other faces is defined relative to the back face of the respective virtual sensor, as shown in Figure 10b. The angles shown in the figure are defined according to the geometry of the lifters and the ring. Due to how the lifters are installed in the ring (Figure 10c) it is convenient to define a projected width of the lifter $w_{b,0}$, which represents the width of the base of the lifter if the curvature of the ring did not exist. Doing so allows defining the angles between the centers of the faces with respect to the back face of the lifter as:

$$\gamma = \tan^{-1}\left(\frac{w_{b,0} - h\tan(\alpha)}{D_M - 2h}\right) \tag{8}$$

$$\varepsilon = \tan^{-1}\left(\frac{2w_{b,0} - h\tan(\alpha)}{D_M - h}\right) \tag{9}$$

$$\beta = 2(\varepsilon - \gamma) \tag{10}$$

$$\xi = \frac{\pi}{N_{lft}} + \frac{\beta}{2} \tag{11}$$

For the geometry and number of lifters of the SetupD100, the angles are $\gamma = 1.836°$, $\varepsilon = 4.762°$, $\beta = 5.853°$ y $\xi = 8.927°$. After locating the different faces of the VS with respect to their corresponding back faces, it is possible to describe the movement of each of the faces of the 3 VS as a function of time, based on the rotation speed of the mill as follows:

$$\theta_{BF,i}(t) = \theta_{0,i} + \omega t \tag{12}$$

$$\theta_{TF,i}(t) = \theta_{BF,i} + \gamma \tag{13}$$

$$\theta_{FF,i}(t) = \theta_{BF,i} + \varepsilon \tag{14}$$

$$\theta_{AL,i}(t) = \theta_{BF,i} + \xi \tag{15}$$

Where ω is the rotation speed of the mill, t corresponds to time, the index $i = 1,2,3$ refers to the virtual sensor and $\theta_{0,i}$ represents the initial position of the back face of the virtual sensor i.

4.2.2 Transformation of forces into local coordinates

Once the location of the 4 faces of the 3 virtual sensors is known as a function of time, it is possible to transform the forces obtained from the virtual sensors from global xy coordinates into local coordinates (normal and parallel) by using the following equations:

For forces acting on the front face:

$$F_{N,FF,i}(t) = F_{x,FF,i}(t)\sin\left(\alpha + \theta_{FF,i}(t)\right) - F_{y,FF,i}(t)\cos\left(\alpha + \theta_{FF,i}(t)\right) \quad (16)$$

$$F_{P,FF,i}(t) = F_{x,FF,i}(t)\cos\left(\alpha + \theta_{FF,i}(t)\right) - F_{y,FF,i}(t)\sin\left(\alpha + \theta_{FF,i}(t)\right) \quad (17)$$

For forces acting on the adjacent liner:

$$F_{N,AL,i}(t) = F_{x,AL,i}(t)\cos\left(\theta_{AL,i}(t)\right) + F_{y,AL,i}(t)\sin\left(\theta_{AL,i}(t)\right) \quad (18)$$

$$F_{P,AL,i}(t) = F_{x,AL,i}(t)\sin\left(\theta_{AL,i}(t)\right) + F_{y,AL,i}(t)\cos\left(\theta_{AL,i}(t)\right) \quad (19)$$

For forces acting on the back face:

$$F_{N,BF,i}(t) = -F_{x,BF,i}(t)\sin\left(\theta_{BF,i}(t)\right) + F_{y,BF,i}(t)\cos\left(\theta_{BF,i}(t)\right) \quad (20)$$

$$F_{P,BF,i}(t) = F_{x,BF,i}(t)\cos\left(\theta_{BF,i}(t)\right) + F_{y,BF,i}(t)\sin\left(\theta_{BF,i}(t)\right) \quad (21)$$

For forces acting on the top face:

$$F_{N,TF,i}(t) = F_{x,TF,i}(t)\cos\left(\theta_{TF,i}(t)\right) + F_{y,TF,i}(t)\sin\left(\theta_{TF,i}(t)\right) \quad (22)$$

$$F_{P,TF,i}(t) = F_{x,TF,i}(t)\sin\left(\theta_{TF,i}(t)\right) - F_{y,TF,i}(t)\cos\left(\theta_{TF,i}(t)\right) \quad (23)$$

Figure 11a shows the forces of Figure 9b, acting on the front face of one of the virtual sensors, after the change of coordinates. After the change of coordinates, it is possible to notice that the magnitude of the normal forces acting on the faces of the lifters is significantly larger than that of the parallel forces.

4.1 Separation in force pulses

As observed in Figure 11a, the magnitude of the forces changes from zero to non-zero in consecutive time intervals, a situation that repeats with every rotation of the mill. This is because the VS is not in contact with the particles when it is located between the shoulder and the toe or the point of impact (whatever occurs first) and, therefore, is not subjected to forces during this time interval. Contrary, when the VS is in contact with particles, the force is non-zero. This process of loading and unloading the VSs is approximately periodic so that lifters and liners are subject to similar forces as they pass through the same angular position.

Based on the above, the forces are subjected to a process of pulse separation. A pulse corresponds to a set of the 8 forces (two for each face, normal and parallel) exerted by the particles on one of the virtual sensors

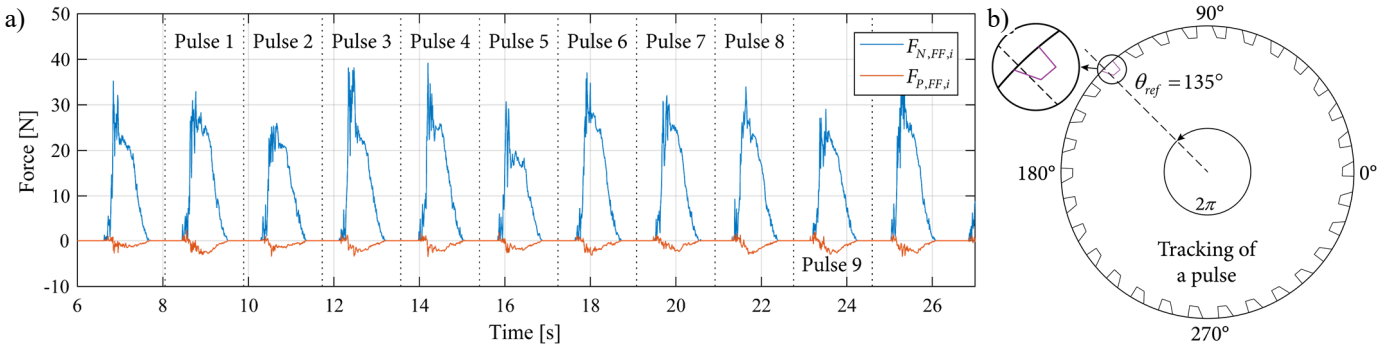

Figure 11: (a) Forces acting on the front face of a SV. Dotted lines mark the beginning and end of the force pulses. (b) Path followed by a SV for pulse separation with reference position of 135°.

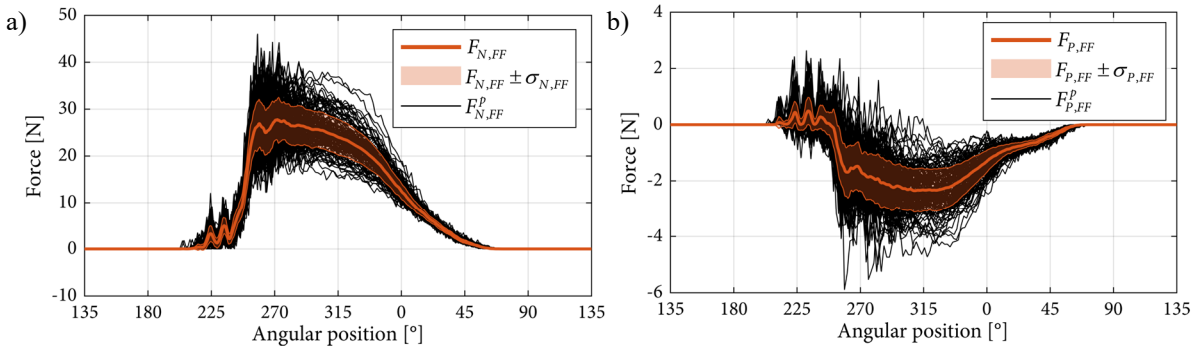

Figure 12: Averaged (red) and individual (black) pulse forces acting on the front face of the lifter. (a) Normal force. (b) Parallel force.

for a complete revolution of the mill around its axis of rotation. The pulse separation allows relating the magnitude of the forces exerted by the particles on the virtual sensors as a function of the angular position instead of time.

The pulse separation is carried out using an algorithm that defines a reference position (θ_{ref}) and identifies the instants of time where the front face of the VS pass through said position. Figure 11b shows the path followed by a VS during which one pulse is obtained, with respect to the reference position (135° in this case). Thus, the pulses correspond to the set of forces exerted by the particles during one rotational period of the mill based on a reference position. In Figure 11a, the vertical dotted lines represent the initial and final time instants of the different pulses. The first pulse is not considered representative because the movement of the load develops only after the first seconds of the simulation.

4.2 Averaging process of pulse forces

Once separated into pulses, the forces are subjected to a process of averaging for deterministic/random separation. The process consists of averaging the magnitude of the pulse forces of the respective faces of the SV when they are in corresponding angular positions. The result of the process is the set of 8 average pulse forces that act on each of the faces of the lifters as a function of the angular position: $F_{N,FF}$, $F_{P,FF}$, $F_{N,AL}$, $F_{P,AL}$, $F_{N,BF}$, $F_{P,BF}$, $F_{N,TF}$ y $F_{P,TF}$. Figure 12a and Figure 12b show, respectively, the average pulse forces $F_{N,FF}$ and $F_{T,FF}$ superimposed on the individual pulses from which they are calculated. Figure 13 shows the forces of Figure 11 (in blue), along with the average force pulses (in red) and the random part of the forces (in yellow). In general, the magnitude of the random part of the forces is low compared to the magnitude of the average forces, especially for normal forces. The average forces represent the stationary forces acting on any of the lifters as

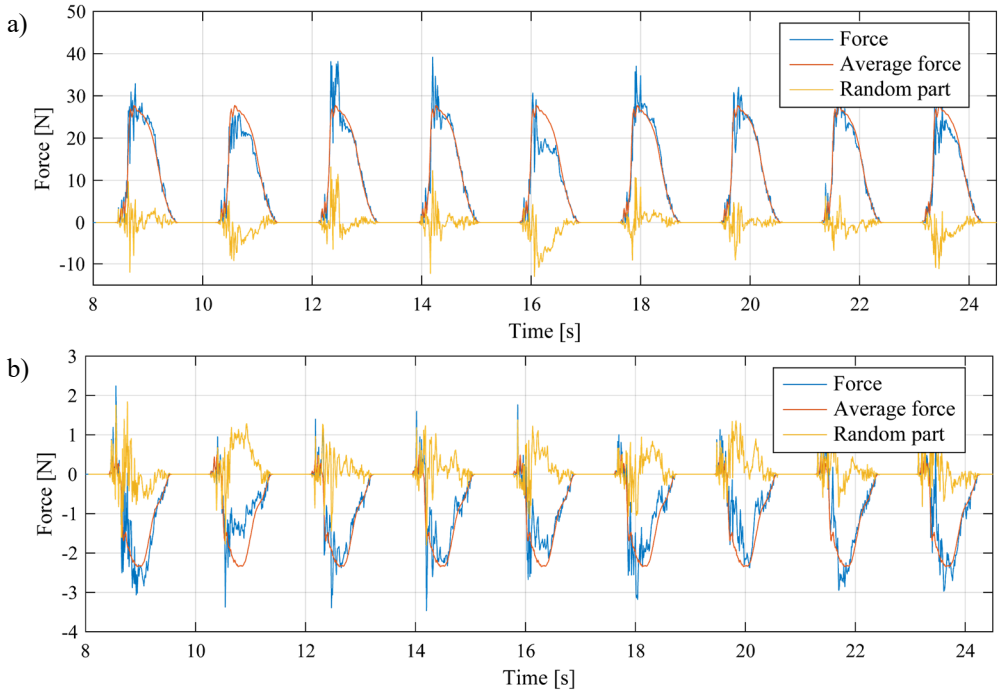

Figure 13: Average/random decomposition of the forces acting on the front face of the lifter. a) Normal force. b) Parallel force.

a function of the angular position, being the random part responsible for deviating the magnitude of the average forces until reaching the magnitude of the individual pulses.

4.3 Calculation of torques and power from the forces acting on the virtual sensors

4.3.1 Time delay of virtual sensor forces

The ring of the mill is composed of a set of liners and lifters, of identical geometry, located in different angular positions. As the VS collect the forces that act on the 3 faces of a lifter and its adjacent liner, it is possible to calculate the power associated with the movement of the ring from the forces they register, assuming that the average forces acting on a lifter i is equal to the forces acting on the reference lifter, when its located in the same angular position.

It is considered that the stationary force acting on each face of a lifter i is equal to the force of the respective face of the reference lifter, including the time delay according to the difference between their angular positions. That is:

$$F_{i,j}(t) = F_{1,j}\left(t - (i-1)T_{lft}\right) \tag{24}$$

Where:

$$T_{lft} = \frac{2\pi}{\omega N_{lft}} \tag{25}$$

N_{lft} is the number of lifters, j represents the force (i.e., face, normal or parallel), i represents the lifter for which the force is being expressed based on the reference lifter on which the stationary force $F_{1,j}$ acts, t is time and T_{lft} is the lifter pass period. Figure 14 illustrates the time delay process, where the forces acting on the rest of the lifters are determined from the forces acting on the lifter 1. Figure 14a shows the result of the phase shift process for 3 lifters. Figure 14b shows the forces acting on all lifters at a given instant, calculated from the average forces acting on the reference lifter.

4.3.2 Calculation of the driving torque and power

Of the eight forces shown in Figure 8, five of them have tangential components and, therefore, exert torques in the direction of rotation of the mill. This set of forces is determinant in the driving torque and, thus, in the

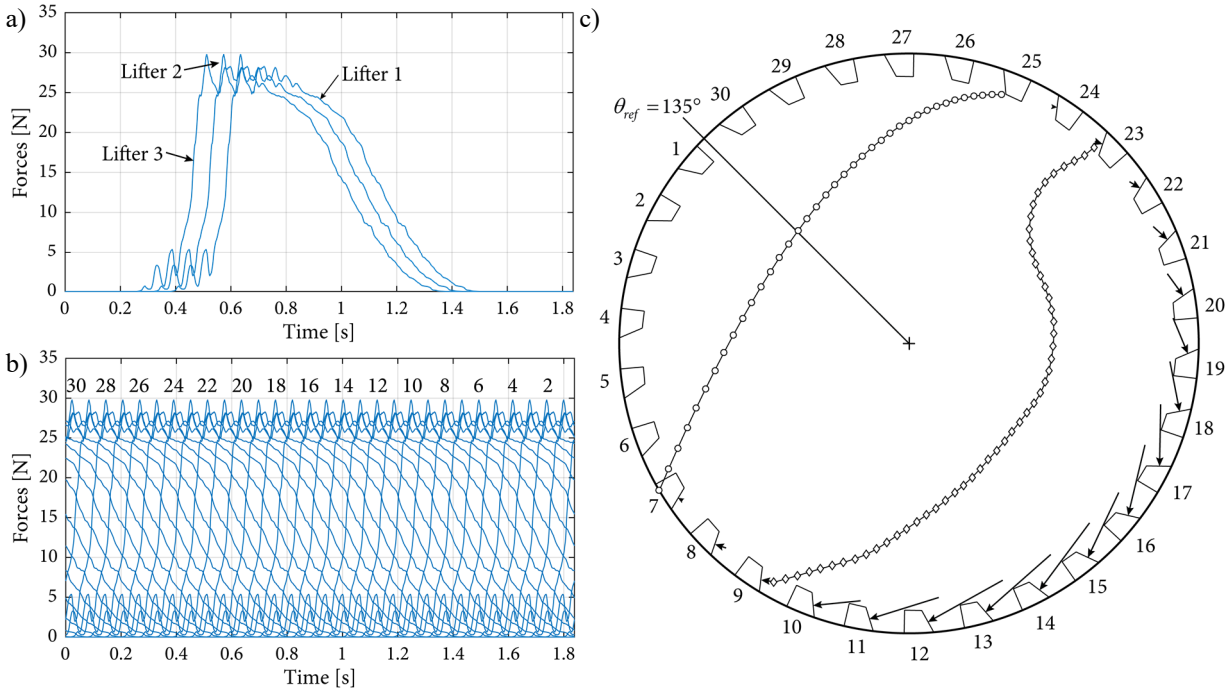

Figure 14: Illustration of the time delay process for determining the forces acting on all lifters and liners. (a) Time delay for three lifters. (b) Time delay for all lifters. (c) Global representation of the forces.

power consumption. Of these five forces, four exert resistant torques, as shown in Figure 6. The force $F_{N,BF}$, acting on the back face of the lifter, exerts torque in the rotation direction, thus favoring the mill's movement and diminishing the required driving torque. As the forces are treated separately for each face, it is possible to obtain the torque associated with the front face, top face, back face, and adjacent liner independently. These torques consider the total number of lifters, due to the time delay process explained in the previous section.

The torques exerted by the different forces acting on any face of a single lifter are given by:

$$\vec{T}_{i,j} = \vec{r}_j \times \vec{F}_{i,j} \tag{26}$$

Where $T_{i,j}$ is the torque exerted by force $F_{i,j}$ acting on the face j of the lifter i, and r_j is the arm of this force. Hence, the torques associated with the different forces acting on each of the faces of a lifter i are given by:

For normal and tangential forces acting on the front face of the lifter (FF):

$$T_{FF,i} = \left(F_{N,FF,i}\cos(\alpha) + F_{P,FF,i}\sin(\alpha)\right)\left(0.25D_M\left(1+\cos(\beta)\right) - h\right) \tag{27}$$

For the tangential force acting on the adjacent lifter (AL):

$$T_{AL,i} = 0.5F_{P,AL,i}D_M \tag{28}$$

For the normal force acting on the back face of the lifter (BF):

$$T_{BF,i} = -0.5F_{N,BF,i}\left(D_M - h\right) \tag{29}$$

For the tangential force acting on the top face of the lifter (TF):

$$T_{TF,i} = F_{P,TF,i}\left(0.5D_M - h\right) \tag{30}$$

And the total torque contribution per face is obtained by considering the respective torques of all N_{lft} lifters:

$$T_{FF} = \sum_{i=1}^{N_{lft}} T_{FF,i};\ T_{AL} = \sum_{i=1}^{N_{lft}} T_{AL,i};\ T_{BF} = \sum_{i=1}^{N_{lft}} T_{BF,i};\ T_{TF} = \sum_{i=1}^{N_{lft}} T_{TF,i} \tag{31}$$

The total torque per face of the lifter and adjacent liner includes the effect of the magnitude change of the forces and its varying angular position as the mill rotates. The total torques associated with each face, obtained from the set of forces acting on the ring, are shown in Figure 15 as a function of time. The figure also indicates the average values.

Finally, the total power due to the movement of the load inside the mill is given by the sum of the average torques associated to each face:

$$P_{Forces} = \left(\overline{T}_{FF} + \overline{T}_{AL} + \overline{T}_{BF} + \overline{T}_{TF}\right)\cdot\omega \tag{32}$$

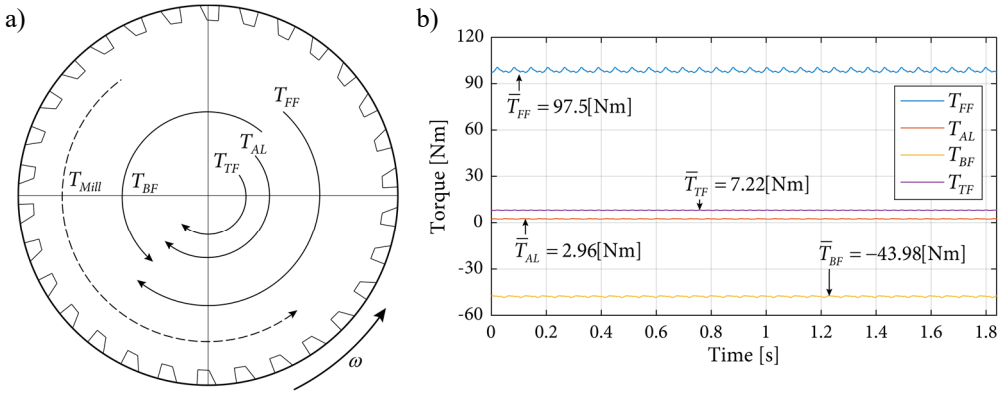

Figure 15: (a) Illustration of the components of the total torque per face of the lifter and adjacent liner. (b) Results of total torque per face as a function of time (average values indicated).

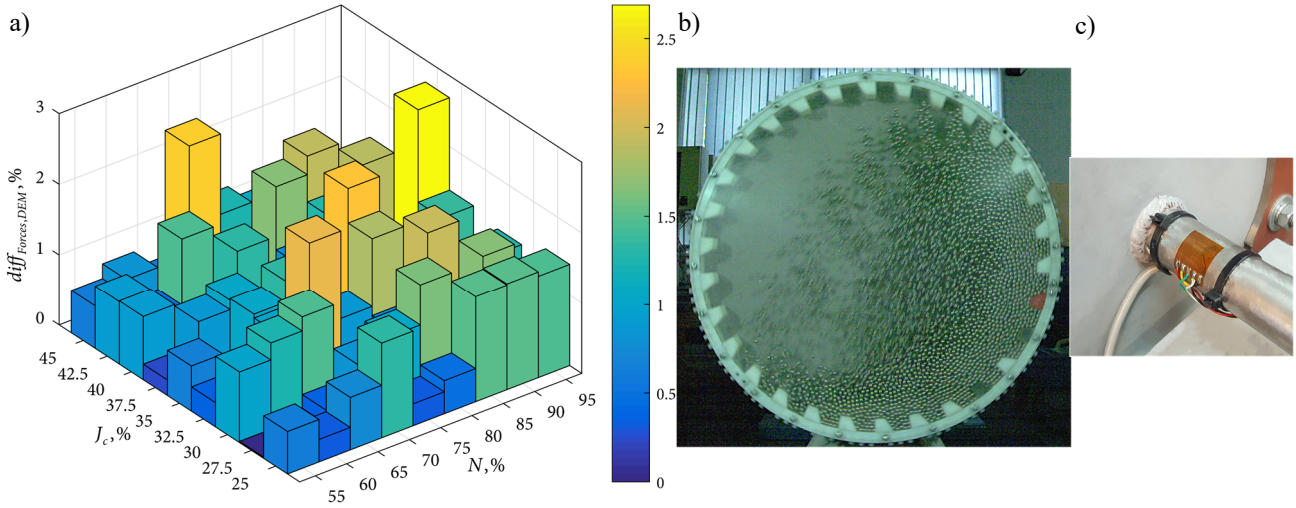

Figure 16: (a) Power differences for different operating conditions. (b) Front view of the mill while operating. (c) Strain gage for experimental measurement of driving torque.

4.3.3 Comparison between the power calculated from the forces and the power obtained from DEM

In order to validate the methodology, the power P_{Forces} is compared to the power $P_{DEM,Ring}$, which is obtained directly from the DEM model of the SetupD100.

Figure 16a shows the difference between the two powers calculated as:

$$diff_{Forces,DEM} = \frac{\left| P_{Forces} - P_{DEM,Ring} \right|}{P_{DEM,Ring}} \tag{33}$$

As observed, the differences between the power obtained directly from the DEM software and the power calculated from the forces are small (maximum 2.69%), thus validating the method to obtain the set of 8 forces as a function of the angular position using the virtual sensors.

5 Instrumentation used in SetupD100

The instrumentation used in SetupD100 focuses on analyzing the movement of the load inside the mill, analyzing the interaction between the lifters and the particles, and the experimental measurement of the power associated with the operation of the mill.

5.1 High-speed camera

One of the main features of the SetupD100 is that it is possible to observe the movement of the particles inside while operating, thanks to its transparent front cover. A high-speed camera (200 fps) is used to record the movement of the load inside the mill. Figure 16b shows an example of the images captured by the camera.

5.2 Driving torque

The measurement of the driving torque is made by using strain gages in full-bridge configuration installed on the mill shaft, between the mill and the bearing, Figure 16c.

The strain measurement in this position allows determining the torque due to the movement of the particles only, eliminating the need to estimate losses in other elements of the powertrain such as couplings and gear transmission. By multiplying the motor torque by the angular speed of the mill, the experimental power associated with the movement of the mill P_{Exp} is obtained, which is equivalent to the power $P_{DEM,Mill}$.

5.3 Instrumented lifter and tachometer

In order to validate the average forces obtained numerically, instrumented lifters resembling the virtual sensors are built. The instrumented lifters are capable of sensing the interaction between the particles and two of the lifter faces: front face (FF) and back face (BF).

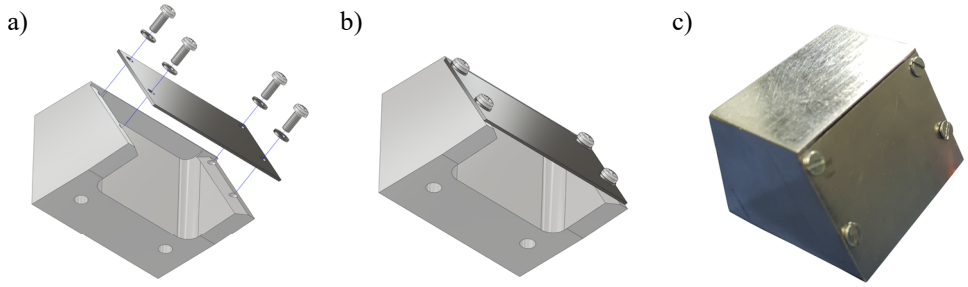

Figure 17: Instrumented lifter for measurement of front face interactions (LI FF). (a) and (b) Assembly. (c) Actual lifter.

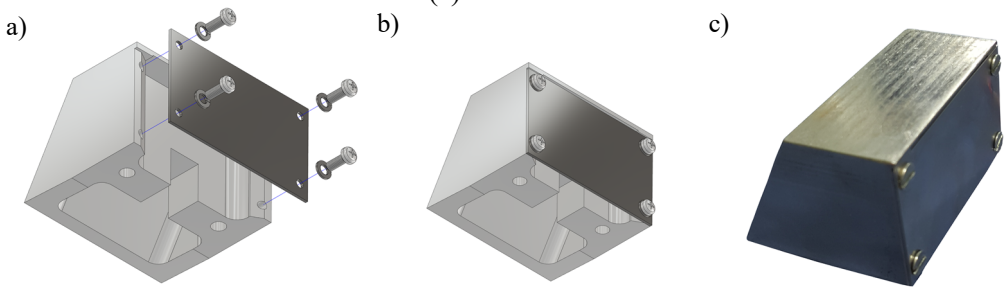

Figure 18: Instrumented lifter for measurement of back face interactions (LI FF). (a) and (b) Assembly. (c) Actual lifter.

The instrumented lifters are composed of two parts: a base block and a thin sensing plate. The sensing plate is made of steel and is fixed to the base block using 4 bolts at its side ends, as shown in Figure 17a. When the instrumented lifter contacts the particles, the sensing plates deflect. The deflection is measured by a pair of bi-axial strain gauges in half bridge configuration installed in the back of the plate. Figure 17 shows the assembly of the instrumented lifter for the measurement of front face interactions (LI-FF); whereas Figure 18 shows the same for measurement of back face interactions (LI-BF).

Figure 19 shows the results of the measurements with the two instrumented lifters for a rotation speed of 75% of the critical speed and a fill level of 30%. As in the case of the forces measured with the VS, the strain measured by the instrumented lifters are separated in pulses. The angular position of the instrumented lifters is determined from the reference signal provided by a photo-tachometer. Subsequently, the experimental pulses (EP) are averaged to obtain an estimator of the stationary component of the pulse forces, Figure 20.

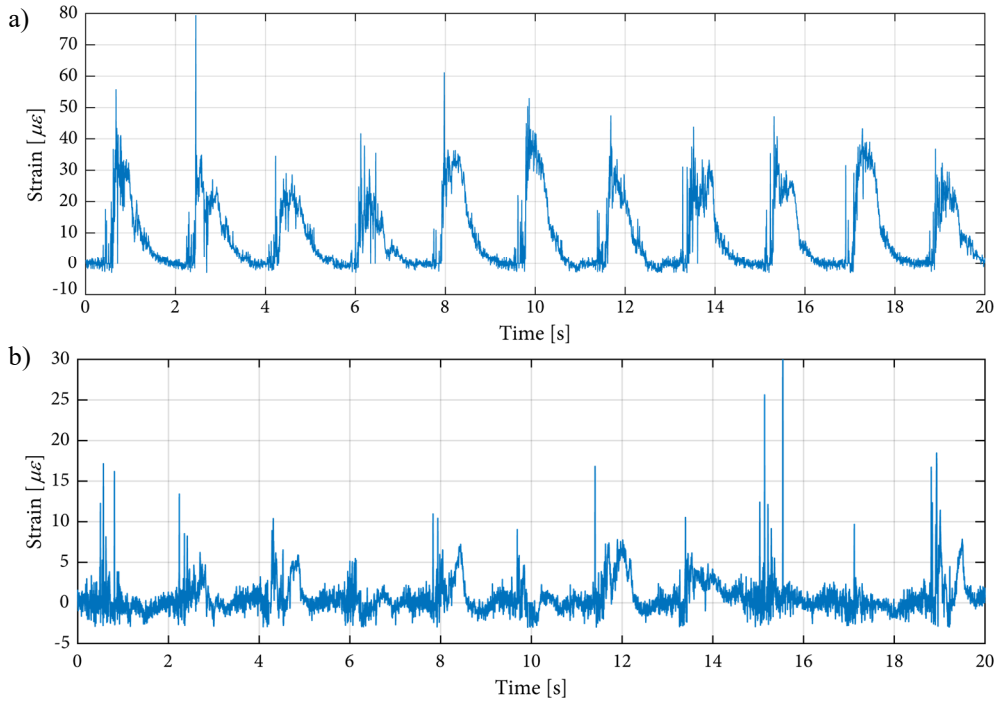

Figure 19: Strain waveform measured by the instrumented lifters. (a) Front face (LI-FF). (b) Back face (LI-BF).

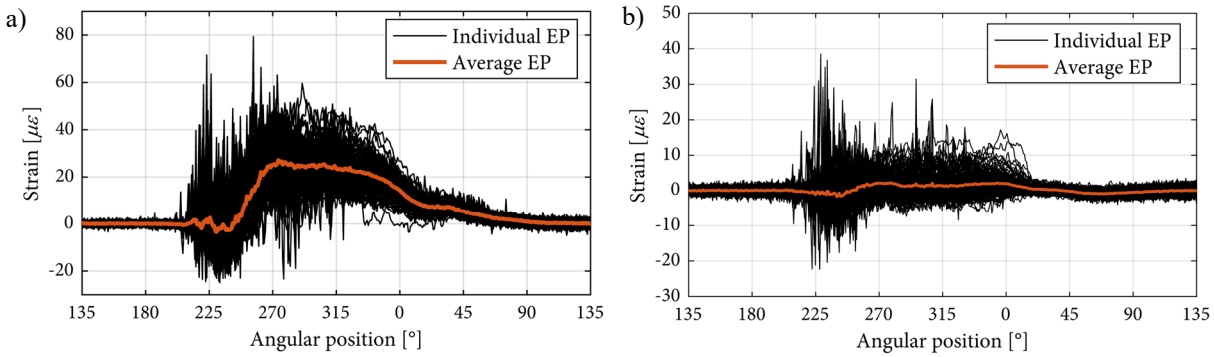

Figure 20: Experimental average pulses obtained with the instrumented lifters. (a) Front face (LI-FF). (b) Back face (LI-BF).

6 Results and discussion

The presented methodology allows a detailed analysis of the behavior of the load inside the mill, which in turn defines the overall behavior of the machine. Of particular interest is the behavior of the power consumption depending on the operating conditions. This behavior has been described in the literature based on the observation of the phenomenon, but a physical explanation has not yet been presented.

This section presents experimental results that validate the proposed methodology. Afterwards, the methodology is used to provide the physical explanation mentioned.

The average forces associated to each face as a function of the angular position, and the corresponding torques they exert, allows analyzing the behavior of the power associated with the movement of the ring from the viewpoint of the interaction of the particles with its internal surfaces.

6.1 Average forces

Figure 21 shows the average forces obtained after processing the forces from the virtual sensors included in the DEM model of the SetupD100, for the mill operating at 75% of its critical speed and a fill level of 30%. As can be observed, the magnitude of the parallel forces is much smaller than the magnitude of the normal forces. Five of the forces acting on the lifter faces are tangential to the ring. From these, the normal forces acting on the front face (FF) and back face (BF) are the most significant in the total torque associated with the rotation of the ring. The 3 remaining forces are parallel forces of magnitude considerably lower than that of normal forces. Based on this, the torque components T_{FF} and T_{BF} are the most relevant in the total torque and thus in the power consumption.

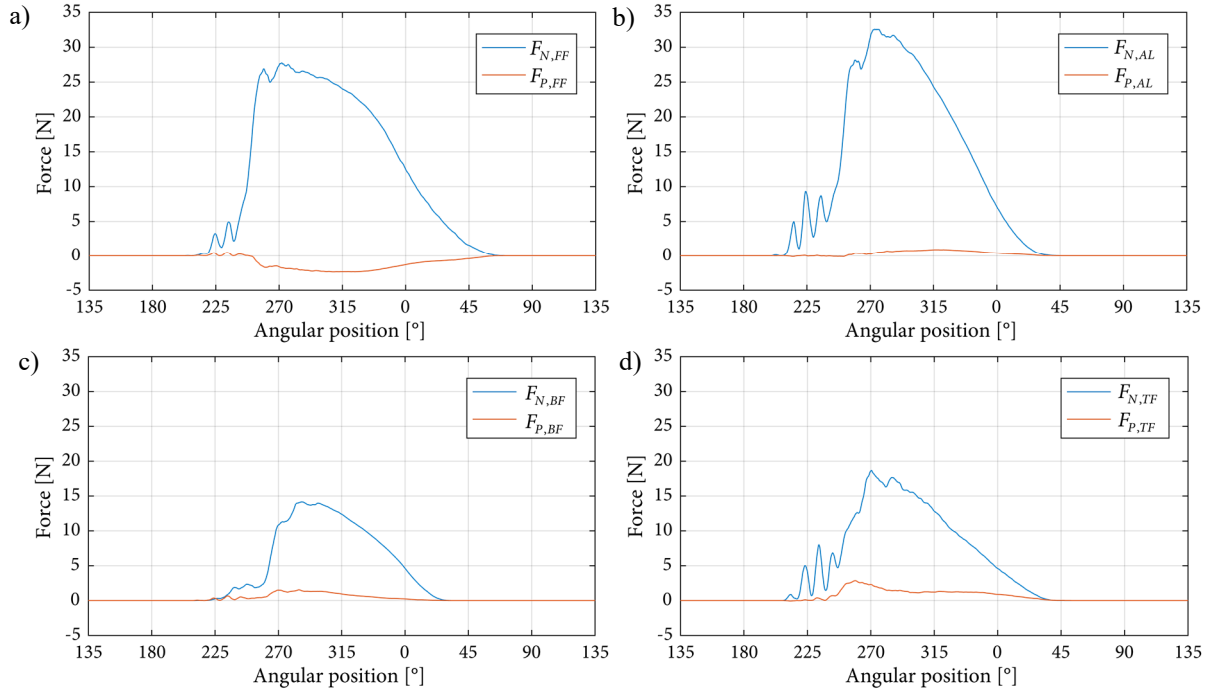

Figure 21: Normal and parallel average forces from the virtual sensors. (a) Front face. (b) Adjacent lifter. (c) Back face. (d) Top face.

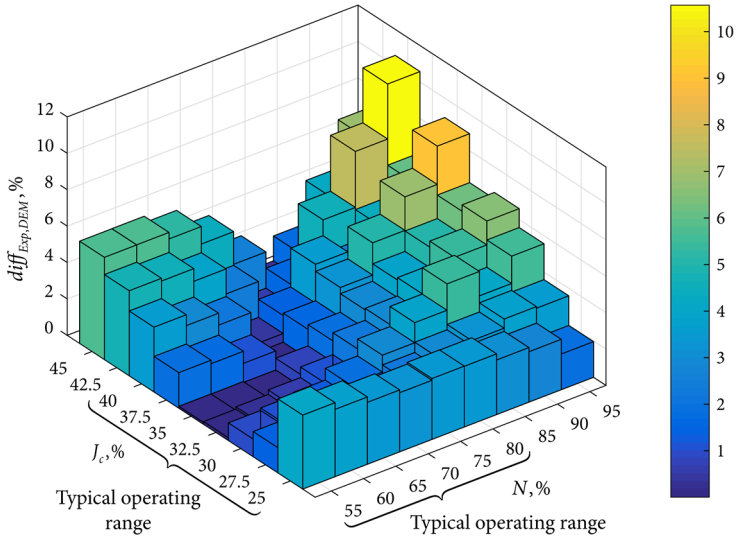

Figure 22: Difference between P_{Exp} and $P_{DEM,Mill}$ for each of the conditions analyzed.

6.2 Experimental validation

The numerical model of the SetupD100 is validated by comparing the numerical results obtained by processing the data extracted from the DEM simulations against their experimental equivalents obtained using the instrumentation of the test bench. The comparison is made first in terms of the power associated with the movement of the mill obtained by DEM ($P_{DEM,Mill}$) and the power obtained experimentally by the strain gauge installed on the drive shaft of the mill (P_{Exp}). As a second approach, the average forces obtained from the virtual sensors and the average experimental pulses obtained with the instrumented lifters are considered. Finally, the disposition of the particles inside the mill obtained by DEM and by the high-speed camera are contrasted.

Figure 22 shows the difference between P_{Exp} and $P_{DEM,Mill}$, calculated as:

$$diff_{Exp,DEM} = \frac{\left| P_{DEm,Mill} - P_{Exp} \right|}{P_{Exp}} \tag{34}$$

The maximum difference is 10.5% for the mill operating at 95% of its critical speed and 42.5% fill level. In mining industries, grinding mills typically operate with speeds ranging between 55% to 80% of the critical speed and fill levels between 25% to 40% of the internal volume. Within this range of operating conditions, the difference between the numerical and experimental power is less than 5%.

Figure 23 shows the comparison between the forces $F_{N,FF}$ and $F_{N,BF}$, and the experimental average pulses obtained with the LI-FF and the LI-BF, for different operating conditions. The differences observed are due to the fact that the instrumented lifters do not measure the contact forces directly, but the strain caused by these forces. Even though the strain is a consequence of these forces, there is no direct relation to the resultant force magnitude, because the force distribution has an influence too. It can also be seen that the magnitude of the measurements made with the LI-BF is much lower than those obtained with the LI-FF. Despite this, there is a clear agreement between the angular intervals in which the forces and the average experimental pulses are non-zero. Also, the fact that the average experimental pulse obtained with LI-BF is mostly positive confirms that the forces exerted by the particles on the BF compress it, generating torques in the sense of rotation of the mill.

Figure 24 compares the disposition of particles inside the mill obtained numerically and experimentally for 3 different operating conditions, showing good correlation.

Based on the similarities observed between the numerical and experimental results, it is reasonable to assume that the numerical model of the SetupD100 and the proposed methodology are valid.

6.3 Effect of rotating speed on the power, torque, and forces

Figure 25a shows the behavior of the power $P_{DEM,Ring}$ as a function of the speed, for the mill operating with different fill levels. Figure 25b shows the same for the torque $T_{DEM,Ring} = P_{DEM,Ring} / \omega$. This torque is equivalent to the sum of the torques $\overline{T}_{FF}$, $\overline{T}_{AL}$, $\overline{T}_{BF}$ and $\overline{T}_{TF}$. It can be seen that the power increases steadily, for all fill levels,

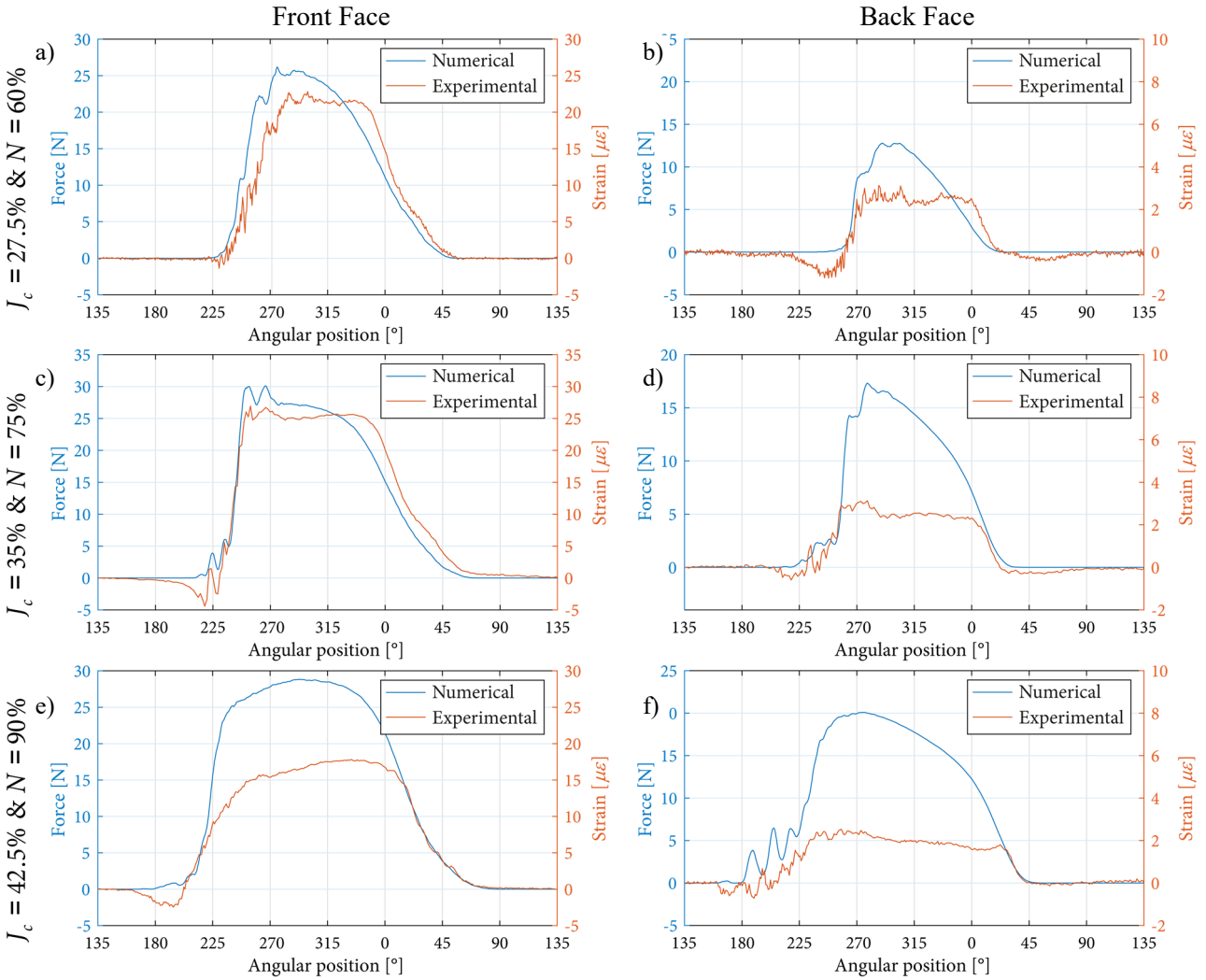

Figure 23: Comparison of numerical and experimental average pulses for the front face and back face, and different operating conditions.

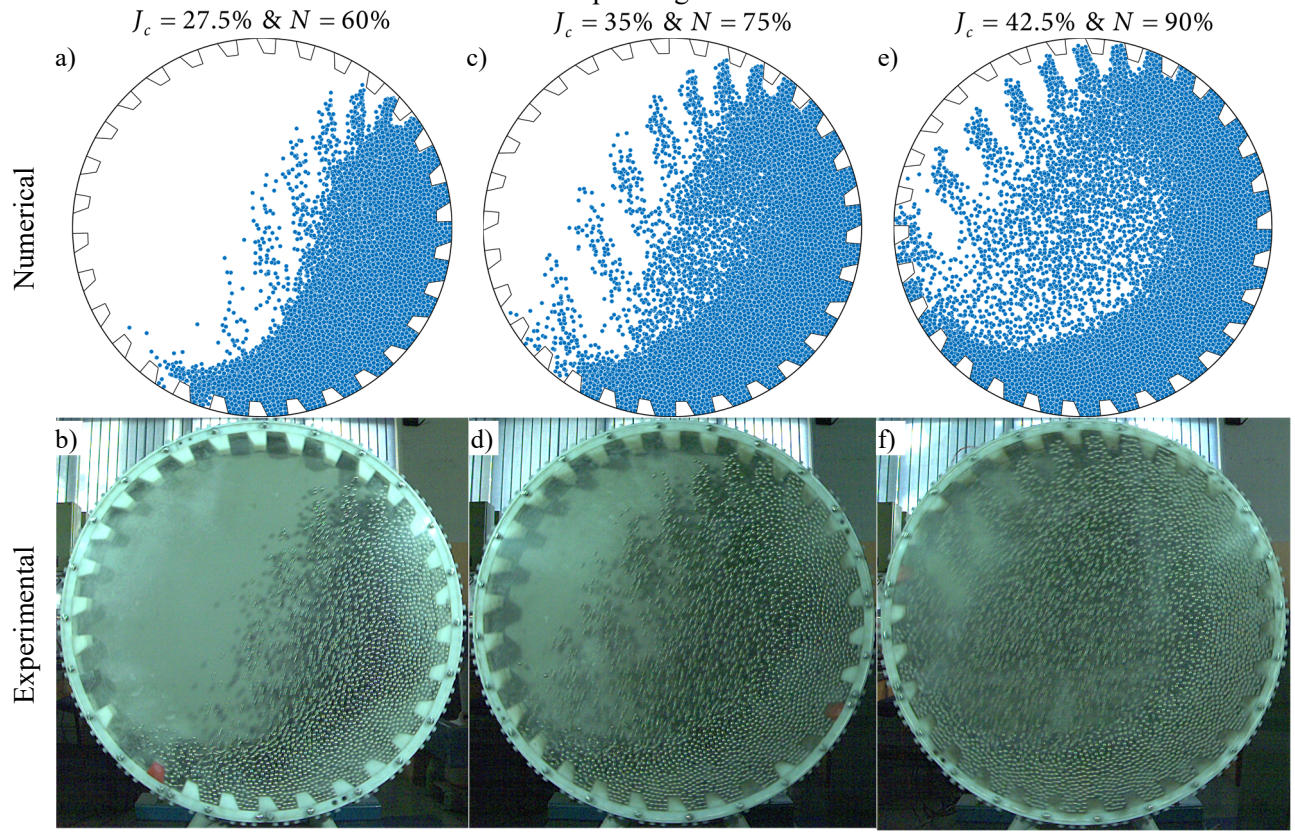

Figure 24: Disposition of particles inside the mill (a),(c),(e) Numerical results. (b),(d),(f) Expermiental results.

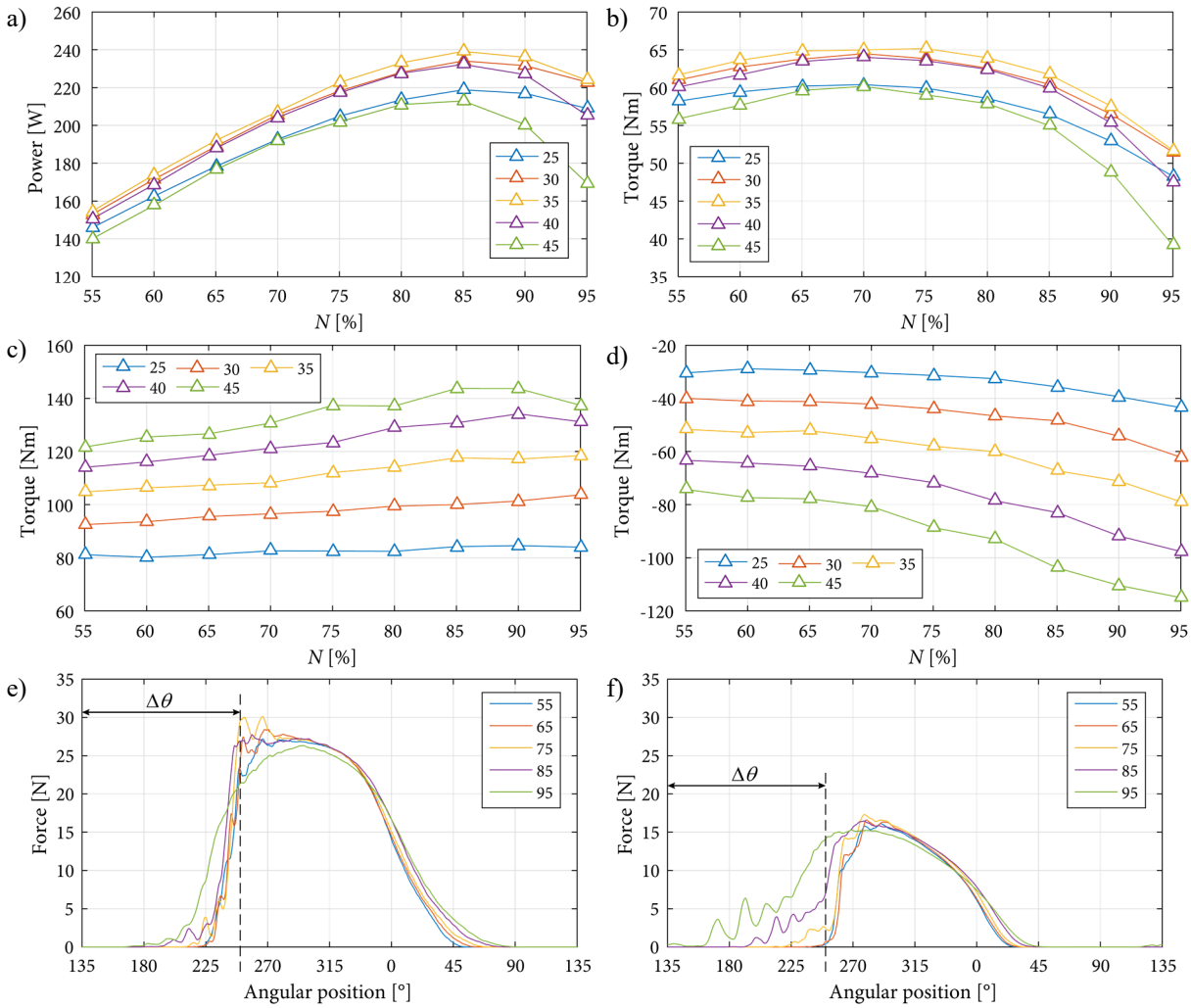

Figure 25: (a) Power $P_{DEM,Ring}$ as a function of speed. (b) Torque $T_{DEM,Ring}$ as a function of speed. (c) Torque T_{FF} as a function of speed. (d) Torque T_{BF} as a function of speed. (e) Force $F_{N,FF}$ as a function of the angular position. (f) Force $F_{N,BF}$ as a function of the angular position.

from 55% to 80% of the critical speed. For higher speeds, the power decreases at a rate that becomes more pronounced as the fill level increases. The torque $T_{DEM,Ring}$ increases up to 70% of the critical speed. From this point on, it begins to decrease. This behavior has been reported in the literature [13][14][21][57], and in order to explain it, the torques and the average forces associated with the different faces of the lifters are further analyzed.

Figure 25c and Figure 25d show the behavior of the torques T_{FF} and T_{BF} as a function of the speed. It can be seen that in the range between 55% and 70% of the critical speed, the increase rate in the magnitude of T_{FF} is slightly higher than the increase rate in the magnitude of T_{BF}, which explains the increase in the magnitude of $T_{DEM,Ring}$ within this speed range. For speeds above 70% of the critical speed, it can be noted that the magnitude of T_{BF} increases at a higher rate than the magnitude of T_{FF}, and that this is more pronounced for higher fill levels. This indicates that the drop in the torque $T_{DEM,Ring}$ for speeds higher than 70% of the critical speed observed in Figure 25b originates because the magnitude of the force $F_{N,BF}$ increases more significantly than the magnitude of the force $F_{N,FF}$ as the rotating speed increases.

Figure 25e and Figure 25f show, respectively, the magnitude of the forces $F_{N,FF}$ and $F_{N,BF}$ as a function of the angular position for the mill operating at 35% of fill level and speed from 55% to 95% of the critical speed with 10% jumps. It can be noted that the magnitude of $F_{N,FF}$ and the angular interval where this force is non-zero increase slightly as a function of the speed of rotation, which produces the slight and sustained increase in the magnitude of T_{FF} observed in Figure 25c. On the other hand, the force $F_{N,BF}$ remains approximately constant between 55% and 65% of the critical speed but begins to increase in the angular range $\Delta\theta$ between 135° and 250° for fill levels above 75%. This behavior originates the increase suffered by the magnitude of

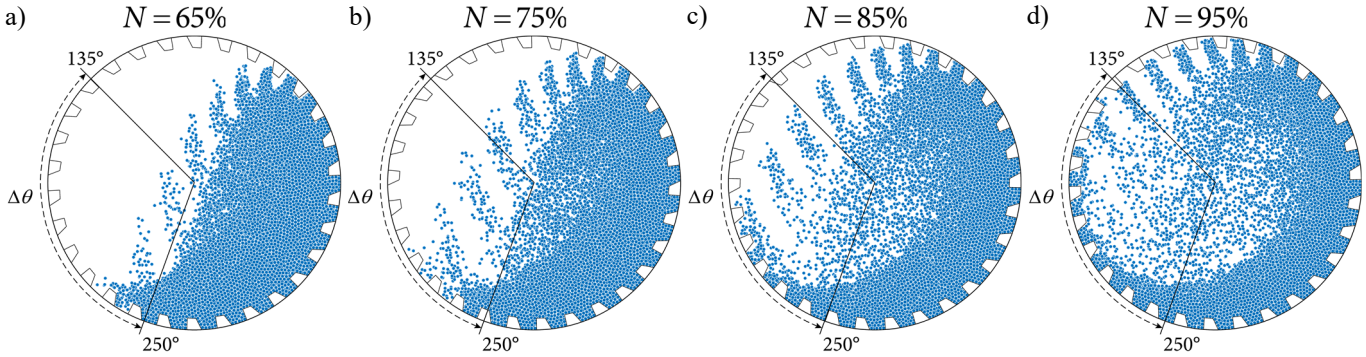

Figure 26: Disposition of particles inside the mill operating with 35% fill level and rotating speed of (a) 65%, (b) 75%, (c) 85% and (d) 95% of the critical speed.

T_{BF} between 70% and 95% of the critical speed, and that causes the decrease of $T_{DEM,Ring}$ in this speed range. The physical phenomenon that gives rise to the forces exerted by the particles in the angular interval between 135° and 250°, for speeds higher than 70% of the critical speed—and that is accentuated with speed--, corresponds to the impact of the particles describing cataract movements and that fall over the toe position, as shown in Figure 26. The particles impacting the internal surface of the mill over the position of the toe exert forces on the back face of the lifters and not on the front face, due to their orientation relative to the path of the particles. These forces exert torques in the sense of rotation of the mill, thus diminishing the total torque requirement. This phenomenon becomes more significant as the rotation speed increases, because both the number and speed of the particles falling on the back face of the lifters above the toe position, increase.

6.4 Conclusions

A methodology is proposed to obtain the magnitude of the average forces exerted by the particles inside the mill on the different faces of the lifters and liners of the ring as a function of their angular position, and the torques associated with each of these faces for the complete set of lifters in the ring. The results obtained from the numerical modeling are in agreement with the corresponding experimental measurements obtained in the test bench, thus validating the methodology.

The forces and torques provide a useful tool to understand the behavior of the power consumed by the mill depending on its geometry and operating conditions. These variables provide the link between the behavior of the load inside the drum and the resulting behavior of the power consumption of the mill. This is especially relevant considering that the energy costs associated with the operation of tumbling mills and the evolution of their internal geometry due to wear, represent a significant fraction of the costs associated with the refinement of minerals.

The results of the analyses carried out in this work show that the decrease in power consumption observed when the speed of the mill increases is due to the impacts of the particles falling on the zone of the ring above the toe of the load. These impacts exert forces on the back face of the lifters, thus increasing the torque component associated with this face, which acts in the sense of rotation. At the same time, as the speed increases, the torque associated with the front face of the lifters also increase, but its magnitude grows at a lower rate. This difference in the growth rates of both torques provides the physical explanation of the power consumption drop at higher speeds.

The methodology seems to be a promising tool in view of gaining further insight about the behavior of tumbling mills and could be useful, for example, to develop strategies to reduce O&M costs and increase efficiency.

References

[1] 'The world's largest sag mill', Outotec, South East Asia Pacific Output, Dec. 2012, page 6.

[2] Guerrero, V. & Pontt, J. 2011. 'Oscillatory Torque Caused by Dead Time in the Current Control of High Power Gearless Mills', *IECON 2011* - 37th Annual Conference on IEEE Industrial Electronics Society, 2011, pp. 1966 – 1970.

[3] Martins, S., Li, W., Radziszewski, P., Faucher, A. & Makni, S. 2013. 'Experimental and simulated instrumented ball in a tumbling mill - A comparison'. *Minerals Engineering*, vol. 43-44, pp.79-84.

[4] Hosseini, P., Martinsm S, Martin, T. Radziszewski, P. & Boyer, F. 2011. 'Acoustic emissions simulation of tumbling mills using charge dynamics'. *Minerals Engineering*, vol. 24, pp. 1440-1447.

[5] Cleary, P., Morrison, R. & Morrell, S. 2003. 'Comparison of DEM and experiment for a scale model SAG mil'. *International Journal of Mineral Processing*, vol. 68, pp. 129-165.

[6] Cleary, P. & Morrison, R. 2016. 'Comminution mechanisms, particle shape evolution and collision energy partitioning in tumbling mills'. *Minerals Engineering*, vol. 86, pp. 75-95.

[7] Cleary, P. 2015. 'Prediction of coupled particle and fluid flows using DEM and SPH'. *Minerals Engineering*, vo. 73, pp. 85-99.

[8] Owen, P. & Clearly, P. 2015. 'The relationship between charge shape characteristics and fill level and lifter height for a SAG mill'. *Minerals Engineering*, vol. 83, pp. 19-32.

[9] Cleary, P. & Morrison, R. 2011. 'Understanding fine ore breakage in a laboratory scale ball mill using DEM'. *Minerals Engineering*, vol. 24, pp. 352-366.

[10] Kalala, J., Breetzke, M. & Moys, H. 2008. 'Study of the influence of liner wear on the load behaviour of an industrial dry tumbling mill using the Discrete Element Method (DEM)'. *International Journal of Mineral Processing*, vol. 86, pp. 33-39.

[11] Powell, M. & McBride, A. 2004. 'A three-dimensional analysis of media motion and grinding regions in mills'. *Minerals Engineering*, vol. 17, pp. 1099-1109.

[12] Mishra, B. 2003. 'A review of computer simulation of tumbling mills by the discrete element method: Part I-contact mechanics'. *International Journal of Mineral Processing*, vol. 71, pp. 73-93.

[13] Cleary, P. 2001. 'Charge behaviour and power consumption in ball mills: Sensitivity to mill operating conditions, liner geometry and charge composition'. *International Journal of Mineral Processing*, vol. 63, pp. 79-114.

[14] Cleary, P. 1998. 'Predicting charge motion, power draw, segregation and wear in ball mills using discrete element methods'. *Minerals Engineering*, vol. 11, pp. 1061-1080.

[15] Mishra, B. & Rajamani, R. 1992. 'The discrete element method for the simulation of ball mills'. *Applied Mathematical Modelling*, vol. 16, pp. 598-604.

[16] Kalala, J & Moys, M. 2004. 'Discrete element method modelling of liner wear in dry ball milling'. *Journal of The South African Institute of Mining and Metallurgy*, vol. 104, pp. 597-602.

[17] Morrison, R. & Cleary, P. 2004. 'Using DEM to model ore breakage within a pilot scale SAG mil'. *Minerals Engineering*. Vol. 17, pp. 1117-1124.

[18] Jiménez-Herrera, N., Barrios, G. & Tavares, L. 2017. 'Comparison of breakage models in DEM in simulating impact on particle beds'. *Advanced Powder Technology*, vol. 29, pp. 692-706.

[19] Cleary, P., Sinnott, M. & Pereira, G. 2015. 'Computational prediction of performance for a full scale Isamill: Part 1 - Media motion and energy utilisation in a dry mill'. *Minerals Engineering*, vol. 79, pp. 220-238.

[20] Tuzcu, E. & Rajamani, R. 2011. 'Modeling breakage rates in mills with impact energy spectra and ultra fast load cell data'. *Minerals Engineering*, vol. 24, pp. 252-260.

[21] Cleary, P. 2001. 'Recent advances in DEM modelling of tumbling mills'. *Minerals Engineering*, vol. 14, pp. 1295-1319.

[22] Cleary, P. 2001b. 'Modelling comminution devices using DEM'. *International Journal for Numerical and Analytical Methods in Geomechanics*, vol. 25, pp. 83–105.

[23] Cleary, P.W., Sinnott, M. & Morrison, R., 2008. 'DEM prediction of particle flows in grinding processes'. *International Journal for Numerical Methods in Fluids*, vol. 58, pp. 319–353.

[24] Cleary, P. 2015. 'A multiscale method for including fine particle effects in DEM models of grinding mills'. *Minerals Engineering,* vol. 84, pp. 88–99.

[25] Djordjevic, N. 2003. 'Discrete element modelling of the influence of lifters on power draw of tumbling mills'. *Minerals Engineering,* vol. 16, pp. 331–336.

[26] Djordjevic, N., 2005. 'Influence of charge size distribution on net-power draw of tumbling mill based on DEM modelling'. *Minerals Engineering*, vol. 18, pp. 375–378.

[27] Geng, F., Gang, L., Wang, Y., Li, Y. & Yuan, Z., 2015. 'Numerical investigation on particle mixing in a ball mill'. *Powder Technology*, vol. 292, pp. 64–73.

[28] Govender, I., McBride, A. & Powell, M. 2004. 'Improved experimental tracking techniques for validating discrete element method simulations of tumbling mills'. *Experimental Mechanics*, vol. 44, pp. 593–607.

[29] Govender, I., Cleary, P. & Mainza, A., 2013. 'Comparisons of PEPT derived charge features in wet milling environments with a friction-adjusted DEM model'. *Chemical Engineering Science,* vol. 97, pp. 162–175.

[30] Hlungwani, O., Rikhotso, J., Dong, H., Moys, M.H., 2003. 'Further validation of DEM modeling of milling: effects of liner profile and mill speed'. *Minerals Engineering,* vol. 16, pp. 993– 998.

[31] Kalala, J., Bwalya, M & Moys, M. 2005. 'Discrete element method (DEM) modelling of evolving mill liner profiles due to wear Part II. Industrial case study'. *Minerals Engineering,* vol. 18, pp. 1386–1391.

[32] Makokha, A & Moys, M. 2006. 'Towards optimising ball-milling capacity: effect of lifter design'. *Minerals Engineering* ,vol. 19, pp. 1439–1445.

[33] Mayank, K., Malahe, M., Govender, I. & Mangadoddy, N. 2015. 'Coupled dem-cfd model to predict the tumbling mill dynamics'. *Procedia IUTAM*, vol. 15, pp. 139–149.

[34] Mishra, B. & Rajamani, R. 1994a. 'Simulation of charge motion in ball mills. Part 1: experimental verifications'. *International Journal of Mineral Processing,* vol. 40, pp. 171–186.

[35] Mishra, B. & Rajamani, R. 1994b. 'Simulation of charge motion in ball mills. Part 2: numerical simulations'. *International Journal of Mineral Processing*, vol. 40, 187–197.

[36] Morrison, R. & Cleary, P. 2008. 'Towards a virtual comminution machine'. *Minerals Engineering*, vol. 21, pp. 770–781.

[37] Mulenga, F. & Moys, M. 2014. 'Effects of slurry filling and mill speed on the net power draw of a tumbling ball mill'. *Minerals Engineering*, vol. 56, pp. 45–56.

[38] Powell, M. & McBride, A. 2006. 'What is required from DEM simulation to model breakage in mills?' *Minerals Engineering*, vol. 19, pp. 1013–1021.

[39] Powell, M., Weerasekara, N., Cole, S., LaRoche, R. & Favier, J. 2011. 'DEM modelling of liner evolution and its influence on grinding rate in ball mills'. *Minerals Engineering,* vol. 24, pp. 341–351.

[40] Rezaeizadeh, M., Fooladi, M., Powell, M., Mansouri, S. & Weerasekara, N. 2010. 'A new predictive model of lifter bar wear in mills'. *Minerals Engineering*, vol. 23, pp. 1174–1181.

[41] Toor, P., Franke, J., Powell, M., Bird, M. & Waters, T. 2013. 'Designing liners for performance not life'. *Minerals Engineering*, vol. 43, pp. 22–28.

[42] Wang, M., Yang, R. & Yu, A. 2012. 'DEM investigation of energy distribution and particle breakage in tumbling ball mills'. *Powder Technology*, vol. 223, pp. 83–91.

[43] Weerasekara, N., Liu, L. & Powell, M. 2016. 'Estimating energy in grinding using dem modelling'. *Minerals Engineering*, vol. 85, pp. 23-33.

[44] Xu, L., Luo, K. & Zhao, Y. 2018. 'Numerical prediction of wear in SAG mills based on DEM simulations', Powder Technology, vol. 329, pp. 353-363.

[45] Qui, Xx, Potapov, A., Song, M., & Nordell, L. 2001. 'Prediction of Wear of Mill Lifters Using Discrete Element Method', In SAG 2001, University of British Columbia, Vancouver, B.B, Canada, pp. 2–7.

[46] Boemer, D & Ponthot, J. 2017. 'DEM modeling of ball mills with experimental validation: influence of contact parameters on charge motion and power draw', *Computational Particle Mechanics*, vol. 4, pp. 53-67.

[47] Wills, B. & Napier-Munn, T. 2006. 'Wills' Mineral Processing Technology', 7th edn, Elsevier Science & Technology Books.

[48] Tano, K., Pålsson, B. & Sellgren, A. 2005. 'On-line lifter deflection measurements showing flow resistance effects in grinding mills', *Minerals Engineering*, vol. 18, pp. 1077–1085.

[49] Owen, P. & Cleary, P. W. 2015. 'The relationship between charge shape characteristics and fill level and lifter height for a SAG mill', *Minerals Engineering*. vol. 83, pp. 19–32.

[50] Cleary, P. W. & Owen, P. 2018. 'Development of models relating charge shape and power draw to SAG mill operating parameters and their use in devising mill operating strategies to account for liner wear', *Minerals Engineering*. vol. 117, pp. 42–62.

[51] Kalala, J., Bwalya, M. and Moys, M. 2005. 'Discrete element method (DEM) modelling of evolving mill liner profiles due to wear. Part I: DEM validation', *Minerals Engineering*, vol. 18, pp. 1386–1391.

[52] Kalala, J., Bwalya, M. & Moys, M. 2005. 'Discrete element method (DEM) modelling of evolving mill liner profiles due to wear. Part I: DEM validation', *Minerals Engineering*, vol. 18, pp. 1386–1391.

[53] Jonsén, P., Pålsson, B. & Häggblad, H. 2012. 'A novel method for full-body modelling of grinding charges in tumbling mills', *Minerals Engineering*, vol. 33, pp. 2–12.

[54] Moys, M., van Nierop, M., van Tondero, J. & Glover, G. 2000. 'Validation of the discrete element method (DEM) by comparing predicted load behaviour of a grinding mill with measured data', *Developments in Mineral Processing,* vol. 13, pp. C3-39-C3-44.

[55] Tano, K. 2005. 'Continuous Monitoring of Mineral Processes with Special Focus on Tumbling Mills – A Multivariate Approach', Doctoral Thesis, Luleå University of Technology.

[56] Tano, K., Pålsson, B. & Sellgren, A. 2005. 'On-line lifter deflection measurements showing flow resistance effects in grinding mills', *Minerals Engineering*, vol. 18, pp. 1077–1085.

[57] Bian, X., Wang, G., Wang, H., Wang, S. & Lv, W. 2017. 'Effect of lifters and mill speed on particle behaviour, torque, and power consumption of a tumbling ball mill: Experimental study and DEM simulation'. *Minerals Engineering*, vol. 105, pp. 22-35.